International Journal of Minerals, Metallurgy and Materials
Volume 30, Number 5, May 2023, Page 802
https://doi.org/10.1007/s12613-022-2554-9

Numerical investigation of the mechanical behavior of the backfill–rock composite structure under triaxial compression

Hongjian Lu✉, *Yiren Wang*, *Deqing Gan*, *Jie Wu*, *and Xiaojun Wu*

School of Mining Engineering, North China University of Science and Technology, Tangshan 063210, China
(Received: 9 June 2022; revised: 25 September 2022; accepted: 26 September 2022)

Abstract: To ensure safe and economical backfill mining, the mechanical response of the backfill–rock interaction system needs to be understood. The numerical investigation of the mechanical behavior of backfill–rock composite structure (BRCS) under triaxial compression, which includes deformation, failure patterns, strength characteristics, and acoustic emission (AE) evolution, was proposed. The models used in the tests have one rough interface, two cement–iron tailings ratios (CTRs), four interface angles (IAs), and three confining pressures (CPs). Results showed that the deformation, strength characteristics, and failure patterns of BRCS under triaxial compression depend on IA, CP, and CTR. The stress–strain curves of BRCS under triaxial compression could be divided into five stages, namely, compaction, elasticity, yield, strain softening, and residual stress. The relevant AE counts have corresponding relationships with different stages. The triaxial compressive strengths of composites increase linearly with the increase of the CP. Furthermore, the CP stress strengthening effect occurs. When the IAs are 45° and 60°, the failure areas of composites appear in the interface and backfill. When the IAs are 75° and 90°, the failure areas of composites appear in the backfill, interface, and rock. Moreover, the corresponding failure modes yield the combined shear failure. The research results provide the basis for further understanding of the stability of the BRCS.

Keywords: backfill–rock composite structure; triaxial compression; mechanical behavior; acoustic emission; numerical simulation

1. Introduction

The mining industry plays a key role in national industrialization and modernization, which promote the rapid development of the national economy [1]. However, mining leads to large amounts of waste tailings and numerous underground cavities [2–4], which exert great pressure on the environment [5–7]. These problems have attracted increasing attention from both the academy and industry [8–10]. Cemented paste backfill (CPB) mining can effectively solve these problems; thus, it has been used worldwide [11–13]. The CPB slurry composed of tailings, water, and binder was thoroughly mixed in the surface filling station and transported underground by pumping or gravity [14–17]. To prevent excess pressure exerted on the barricade, CPB with high strength was first poured into the mined-out area until a certain height was reached, and CPB with low strength was then injected [18]. The slurry consolidated underground achieved a certain strength and coupled with the surrounding rock to form the underground backfill–rock composite structure (BRCS), as shown in Fig. 1. Therefore, the mechanical behavior of BRCS under triaxial compression is of great significance to ensure the safe production of mines.

At present, researchers have made remarkable achievements in the study of the mechanical behavior of backfill–rock combinations [20–23]. Moreover, corresponding research results of rock–concrete [24–25], salt–rock [26–27], and coal–rock [28–30] combinations have been obtained using physical experiments and numerical simulations. However, only a few achievements in the study of the mechanical properties of BRCS have been made. Koupouli *et al.* [31] analyzed the shear characteristics of combinations of backfill and rock and two different strength backfills. Considering the deformation mechanism of the interface and the interaction of asperities, Zhang *et al.* [32] proposed a strength model for backfill–rock combinations with an irregular interface based on fractal theory. By conducting mechanical tests, Xiu *et al.* [33] analyzed the shear mechanical properties of the wet and dry interfaces between CPB and rock. By performing numerical simulations, Falaknaz *et al.* [34] analyzed the mechanical response characteristics of two adjacent backfill stopes. Xu *et al.* [35] conducted uniaxial compression tests of stratified backfills and analyzed their acoustic emission (AE) characteristics. Wu *et al.* [36] investigated the shear strength and deformation of CPB–rock under triaxial compression with interface angles (IAs) of 45° and 60°. Wang *et al.* [19] investigated the strength and failure characteristics of composite samples under uniaxial loading. BRCSs were composed of interfaces, CPBs, and rocks. Notably, the interfaces were sloping and rough (Fig. 1(a)) because of the occurrence conditions and mining methods of ore bodies [19]. However, only a few studies have investigated the tri-

✉ Corresponding author: Hongjian Lu E-mail: luhongjian@ncst.edu.cn

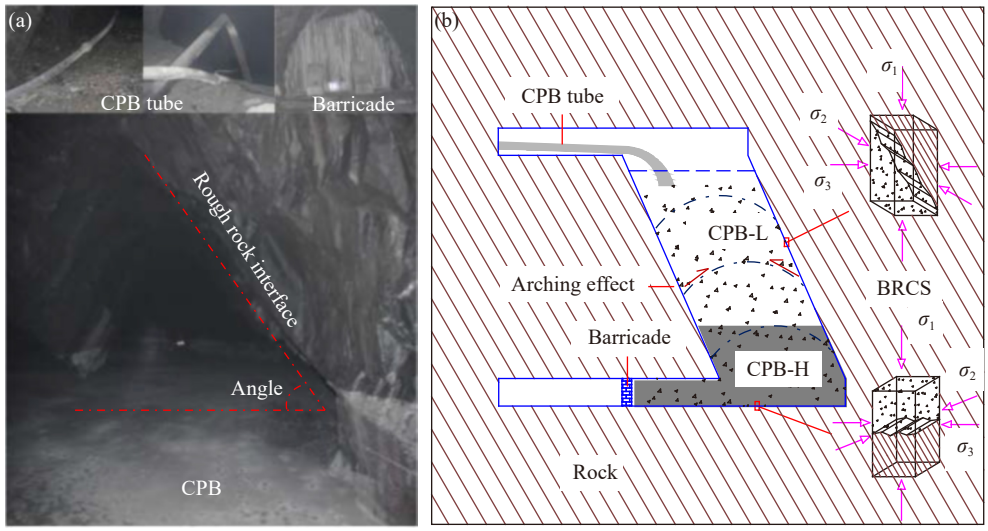

Fig. 1. Backfill–rock composite structure (BRCS) engineering model: (a) cemented paste backfill (CPB) in the mining site; (b) engineering model; CPB-H is CPB with high-strength; CPB-L is CPB with low-strength; σ_1 is vertical stress in *y* direction; σ_2 is horizontal stress in *x* direction; σ_3 is horizontal stress in *z* direction [19].

axial compression mechanical properties of BRCS and considered the aforementioned interface features simultaneously. To reveal the mechanical properties of BRCS under triaxial compression with one rough interface, four IAs, two cement–iron tailings ratios (CTRs), and three confining pressures (CPs), including deformation failure, failure patterns, strength, and AE evolution, corresponding simulation tests were conducted using the 3D Realistic Failure Process Analysis (RFPA^{3D}). The mechanical properties of BRCSs with different nonlinear IAs were systematically investigated by conducting triaxial compression numerical simulation tests. The results can provide further insights into the stability of the backfill–rock interaction system.

2. Experimental

2.1. Triaxial compression analysis method of BRCS

The RFPA^{3D} is a finite element code that can simulate the failure process of rock and CPB [37–38]. The AE counts reflect the cumulative number of damaged elements, and the AE energy reflects the elastic energy released during the damage process of rock and CPB elements [39−40].

The Young's modulus or strength of each finite element is assumed to follow the Weibull distribution:

$$\varphi(u) = \frac{m}{u_0}\left(\frac{u}{u_0}\right)^{m-1} \exp\left[-\left(\frac{u}{u_0}\right)^{m}\right] \tag{1}$$

where u is Young's modulus or strength, u_0 is the corresponding relevant average, and m is the homogeneity coefficient [40–41].

The Mohr–Coulomb criterion and maximum tensile stress criterion are used in RFPA^{3D} [42–43]. The damage variable D is expressed as follows:

$$D = \begin{cases} 0, \varepsilon < \varepsilon_{t0} \\ 1 - \dfrac{\sigma_{tr}}{\varepsilon E_0}, \varepsilon_{t0} \le \varepsilon \le \varepsilon_{tu} \\ 1, \varepsilon > \varepsilon_{tu} \end{cases} \tag{2}$$

where E_0 is the elastic modulus of undamaged elements, σ_{tr} is the residual strength, ε_{t0} is the strain at the elastic limit, and ε_{tu} is the ultimate tensile strain [40].

The Mohr–Coulomb criterion is applied to define the shear damage variable D of elements, which can be expressed as follows [40,44]:

$$D = \begin{cases} 0, \varepsilon < \varepsilon_{c0} \\ 1 - \dfrac{\sigma_{cr}}{\varepsilon E_0}, \varepsilon \ge \varepsilon_{c0} \end{cases} \tag{3}$$

where ε_{c0} is the critical strain and σ_{cr} is the residual shear strength [40].

2.2. Mechanical parameter calibration and model validation

The material meso-parameters in RFPA^{3D} include elastic modulus, uniaxial compressive strength (UCS), homogeneity coefficient (m), compression–tensile strength ratio, friction angle, Poisson ratio, residual strength coefficient, ultimate tensile strain coefficient, and ultimate compressive strain coefficient. The homogeneity coefficient affects the crack development mode and macromechanical behavior, and the residual strength coefficient affects the toughness and bearing capacity of a material [45].

The relationships between the meso-elastic modulus ($\overline{E_0}$) of elements and the macro-elastic modulus (E_0) of BRCSs and between meso-UCS ($\overline{\sigma_0}$) of elements and macro-UCS (σ_0) of BRCSs are expressed as follows:

$$\overline{E_0} = E_0 / C_E \tag{4}$$

$$\overline{\sigma_0} = \sigma_0 / C_S \tag{5}$$

where C_E is the elastic modulus coefficient and C_S is the UCS coefficient. The relationships between m and C_E and between m and C_S are expressed as follows:

$$C_S = 0.2047 \ln m + 0.1156 \tag{6}$$

$$C_E = 0.0813 \ln m + 0.7679 \tag{7}$$

Moreover, the meso-parameters of the two materials of BRCS were accurately calibrated. The correction process is

illustrated in Fig. 2.

Fig. 2 shows the meso-parameters calibration and validation process of the models. The relative errors between numerical calculation results and corresponding experimental results meet the requirements (i.e., <5%) [40], and the results are reasonable.

2.3. Materials and sample parameters

This research is a continuation of a previous study [19]. The tailings used were obtained from an underground iron mine in Hebei Province, China. The rock samples were blue sandstone collected from Changsha, Hunan Province, China, and cut into units. The structure and size of numerical models, CTRs of backfill samples, and composites were consistent with the parameters in the literature.

2.4. BRCS model building method and constraints

The solid models and constraint files were set up from ANSYS and imported into RFPA^{3D} for calculation and analysis. Fig. 3 shows the BRCS numerical models. Each model was set with a length of 50 mm, width of 50 mm, and height of 100 mm. The finite element was set as a regular hexagonal element with a side length of 1.25 mm. Therefore, each model was divided into 128000 units.

The models with IAs of 0° to 90° were used for BRCS parameter calibration and model validation. The models with IAs of 45°, 60°, 75°, and 90° were used for BRCS triaxial compression experiments according to the previous results [19,46], and the triaxial CPs were set as 0.4, 0.8, and 1.2 MPa to approach the in-site backfill lateral stress monitoring data range. The displacement load of 0.03 mm/step was applied to the *y*-direction of the models until destruction. The CPs were applied to the *x*- and *z*-directions.

3. Results

3.1. BRCS parameter calibration and model validation

Table 1 shows the contents of the model calibration and validation tests. Fig. 4 shows the comparisons of the stress–strain curves of the physical experiments and numer-

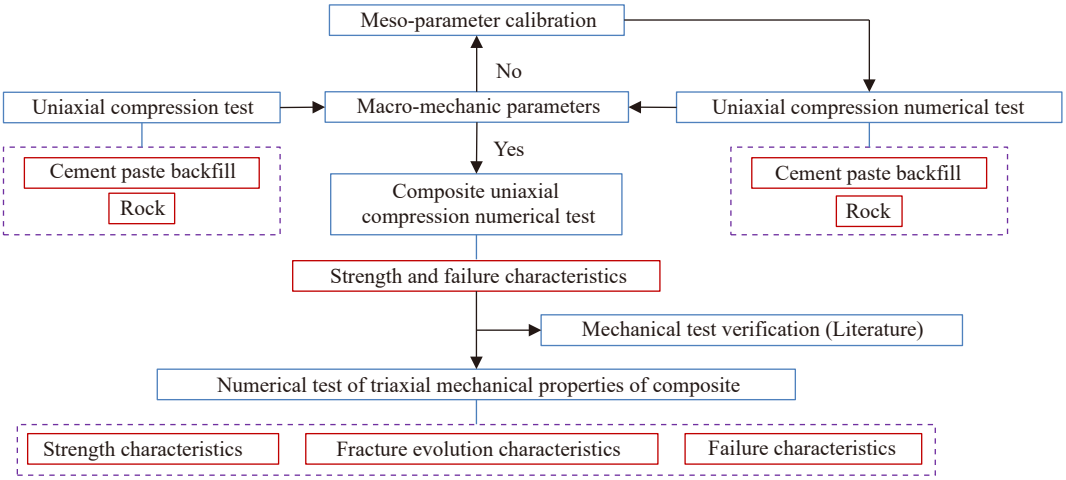

Fig. 2. BRCS meso-parameter calibration and validation process.

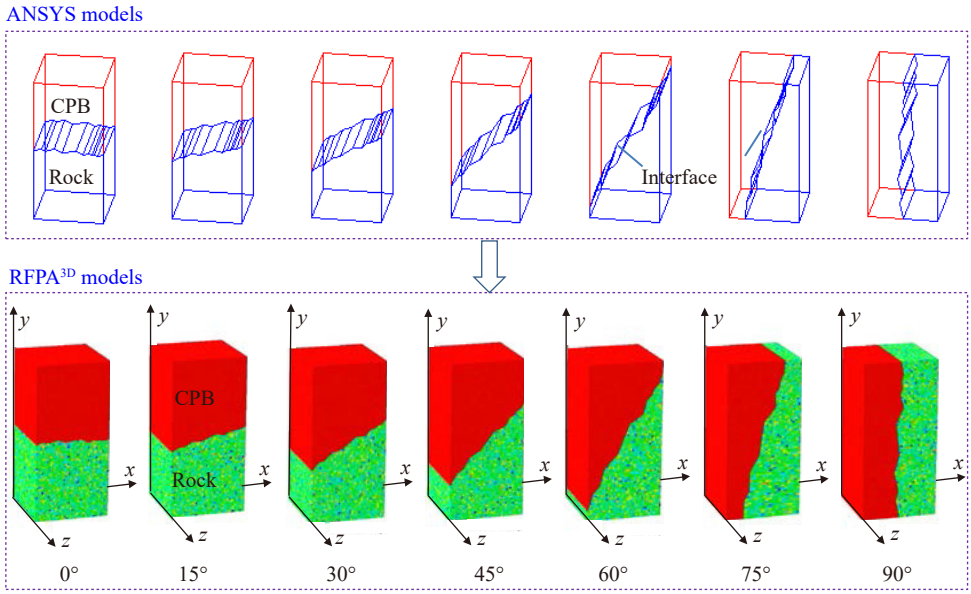

Fig. 3. BRCS numerical test models.

ical simulations. Notably, the stress–strain curves of CPBs and rock in the numerical simulations are nearly identical to those in the physical experiments. The relative errors between numerical and experimental UCS are 3.94% for CPB with CTR 1:8, 2.88% for CPB with CTR 1:4, and 0.81% for rock, which are all <5%. According to the meso-parameter calibration process of BRCS (Fig. S1), the calibrated meso-parameters of CPB and rock were obtained, as listed in Table 2.

Fig. 4 shows the comparisons of the experimental (E) and numerical (N) stress–strain curves of BRCS with different IAs, and they exhibit good similarity. The maximum relative error between numerical and experimental UCS is 1.73%, which indicates the capability of RFPA^{3D} to simulate the mechanical behavior of BRCS test blocks.

3.2. BRCS triaxial compressive deformation characteristics

Fig. 5 and Fig. S2 show the BRCS triaxial compressive stress–strain curves of the numerical tests, which can be divided into five stages, namely, compaction, elasticity, yield, strain softening, and residual stress. CPs were first applied, which ensured that the compaction stage was not obvious. When the IAs are 45° and 60°, the intervals of yield stages

Table 1. Calibration and model validation numerical tests

Type	IAs	CTR	Solid content	Test purpose
CPB		1:4, 1:8	70wt%	Calibration
Rock				Calibration
BRCS	0°, 15°, 30°, 45°, 60°, 75°, 90°	1:4, 1:8	70wt%	Validation

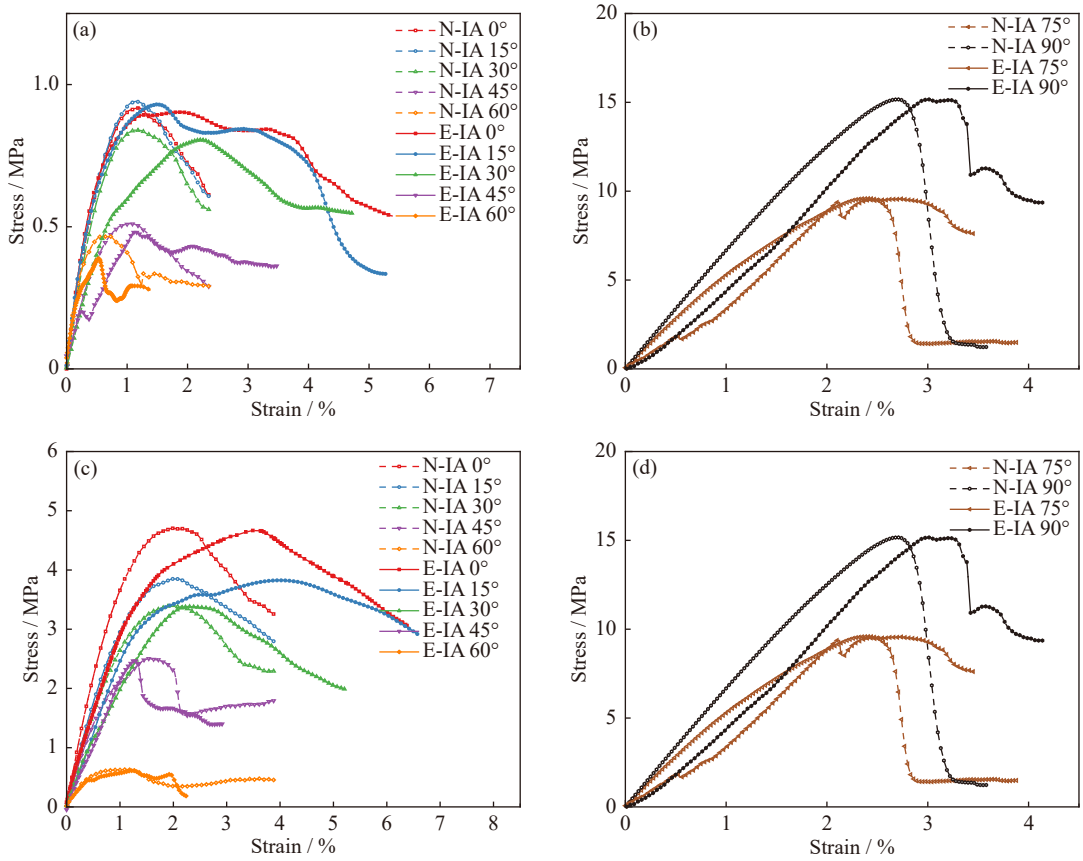

Fig. 4. Comparisons of the stress–strain curves of the numerical simulations and physical experiments of (a, b) BRCS with CTR 1:8 and (c, d) BRCS with CTR 1:4.

Table 2. Meso-parameters of CPB and rock

Sample	*m*	*E* / MPa	UCS / MPa	*φ* / (°)	C-TR	PR	UTC	UCC	RSC
CPB with CTR 1:8	1.00	138.40	8.40	34	12	0.28	5.0	100	0.01
CPB with CTR 1:4	1.20	239.08	16.61	34	10	0.28	5.0	100	0.10
Rock	2.50	3385.60	254.10	36	10	0.25	5.0	100	0.01

Notes: *m* is homogeneity coefficient; *E* is elastic modulus; UCS is uniaxial compressive strength; *φ* is friction angle; C-TR is compression–tensile strength ratio; PR is Poisson ratio; UTC is ultimate tensile strain coefficient; UCC is ultimate compressive strain coefficient; RSC is residual strength coefficient.

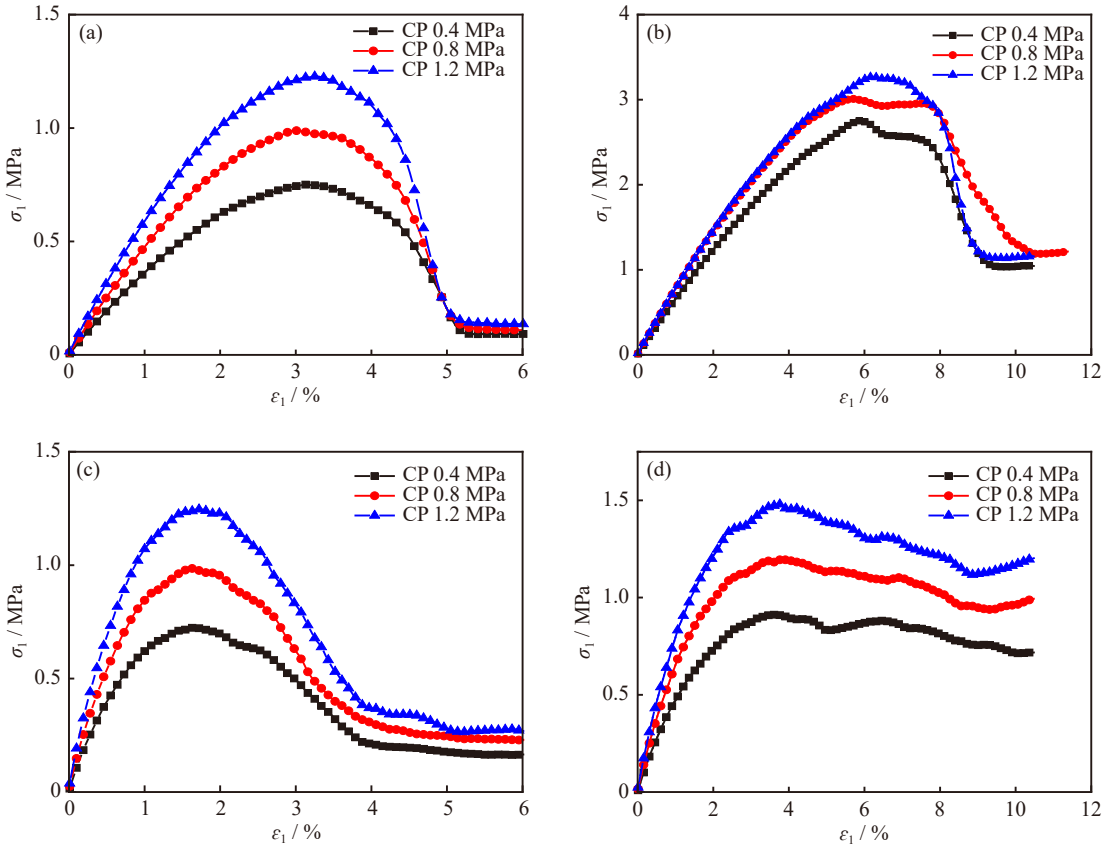

Fig. 5. BRCS triaxial compressive stress–strain curves: (a) CTR 1:8–IA 45°; (b) CTR 1:4–IA 45°; (c) CTR 1:8–IA 60°; (d) CTR 1:4–IA 60°.

are long, the stress peak phenomenon occurs, and the curves of the stress softening slopes are gentle. In particular, when the IA is 60° and the CTR is 1:4, the stress softening slope is gentle, the peak strength is close to the residual strength, and the ductility feature is obvious. When the IAs are 75° and 90°, the intervals of yield stages are short, and the stress peak points are obvious. After the occurrence of the stress peak phenomenon, the strengths of the composites decrease sharply, their residual strengths are far less than the corresponding peak strengths, and brittleness is obvious.

3.3. BRCS triaxial compressive strength characteristics

The Mohr–Coulomb criterion was used as the failure criterion of BRCSs; thus, two parameters, i.e., cohesion and friction angle, are significant to the composite strength [32,35]. Through the linear fitting of maximum principal stress σ_1 and CP σ_3, the characteristic parameters of triaxial compressive strength were obtained, as shown in Table 3.

The triaxial compressive strength of composites with the IA of 90° is the highest, followed by those of composites with IAs of 75°, 45°, and 60°. A good linear relationship between σ_1 and σ_3 was observed, and the correlation coefficient R^2 exceeded 0.97. These findings verify the linear Mohr–Coulomb yield criterion. With the increase of σ_3, σ_1 increases linearly, and the CP strengthening effect of the models occurs. The more the IA increases, the more obvious the CP strengthening effect. Moreover, the change of CTR has only a slight effect on it.

Table 3. Strength characteristic parameters of BRCSs under triaxial compression

CTR	IA / (°)	σ_1 / MPa				K	Q	R^2	φ / (°)	c / MPa
		$\sigma_3 = 0$	$\sigma_3 = 0.4$	$\sigma_3 = 0.8$	$\sigma_3 = 1.2$					
1:8	45	0.512	0.750	0.9905	1.228	0.597	0.512	0.99	31.16	0.331
	60	0.464	0.725	0.986	1.247	0.653	0.464	0.98	31.20	0.287
	75	3.684	4.681	5.678	6.675	2.492	3.684	0.97	31.86	1.167
	90	14.822	17.033	19.245	21.456	5.529	14.822	0.99	32.18	3.152
1:4	45	2.490	2.750	3.010	3.270	0.650	2.490	0.98	31.20	1.544
	60	0.627	0.911	1.195	1.480	0.710	0.627	0.97	31.25	0.372
	75	9.605	10.662	11.719	12.774	2.641	9.605	0.97	31.88	2.956
	90	15.268	17.610	19.951	22.293	5.854	15.268	0.99	32.20	3.155

Notes: K and Q are the strength related parameters; φ is the friction angle; c is the cohesion.

With the increase of the IA, the friction angles of BRCSs slightly increase from 31.16° to 32.18° (CTR of 1:8) and from 31.25° to 32.20° (CTR of 1:4). Meanwhile, their cohesions change significantly. The cohesion of the composite with the IA of 60° is the lowest, whereas that with the IA of 90° is the highest. When the IAs are 60° and 90°, the CTR has only a slight effect on cohesion. By contrast, when the IAs are 45°and 75°, the CTR significantly affects cohesion. Thus, cohesion is sensitive to IA and CTR.

3.4. BRCS triaxial compressive failure evolution analysis

To reveal and analyze the damage growth and distribution processes of BRCSs, the information on their failure evolution with different IAs and the same CP (0.8 MPa) and CTR (1:8), including the AE counts–stress–strain curves, nephograms of the AE points, damage units, and typical stress points of *y* axial displacement, is illustrated in Fig. 6 and Figs. S3 to S5. The damage values 0 and 1 in color sticks represent intact and completely damaged, respectively, and are denoted by red and blue in the displacement color sticks, respectively.

As shown in the compaction and elastic stages of the stress–strain curve, small numbers of AE counts and damaged elements appear at the lower part of the interface because of the coordinated deformation of the two materials. As the *y* axial displacement increases, composite deformation reaches the plastic stage, but the rock part retains a unified displacement, which indicates elastic characteristics. The CPB displacement gradually decreases at the contact interface. Then, the damaged units begin to replace the CPB units and gradually emerge on the interface. The distribution type of AE points transitions from multipoint in the CPB to concentrate on the interface. The crack l_1 extends along the entire interface from top to bottom. During the post-peak stress stage, the composites slide along their interfaces, but the CPBs still have their bearing capacity because of the action of CP and nonlinear interface friction. With the increase of axial displacement, the CPB units that are perpendicular to the interface are intensively damaged, and the crack l_2 is formed. The composite is divided into three displacement change areas by cracks l_1 and l_2. The displacements between the upper half of the CPB and rock are significantly different, the development of cracks (l_{1-2}) and the displacements between the lower half of the CPB and rock are slightly different, and the fracture close (l_{1-1}) and the shape of the crack changes from "y" to "v." In the residual stress stage of the stress–strain curve, the composite bearing capacity becomes small, and crack l_3 extends along the intersection of the "v" flaw.

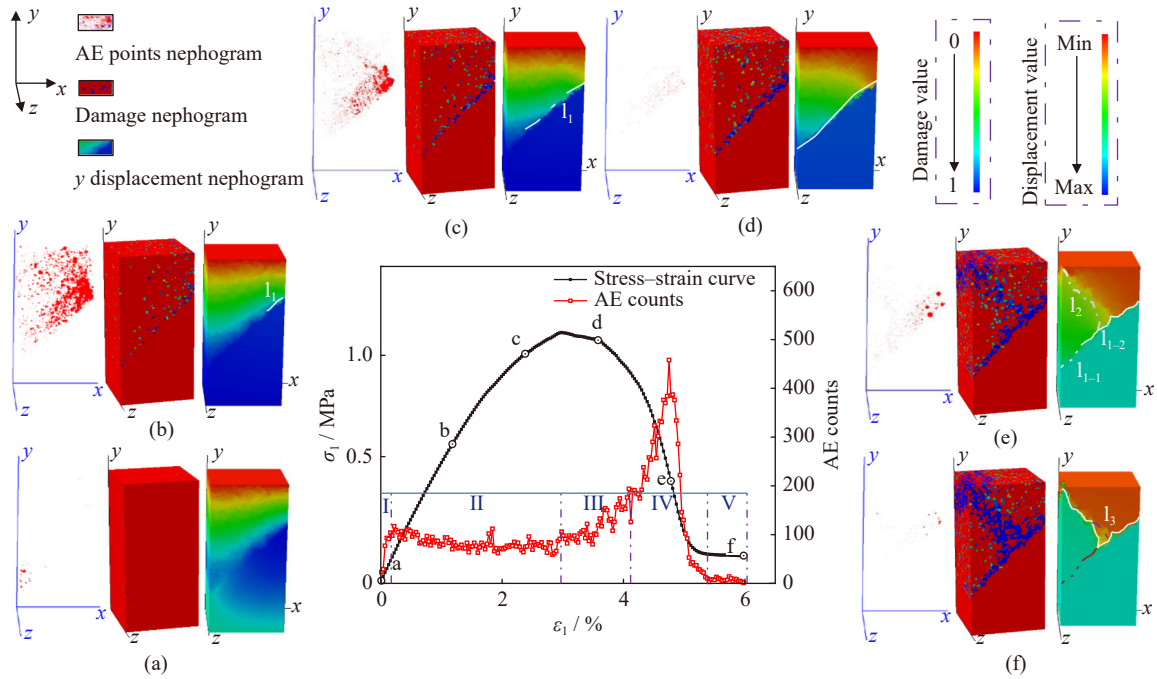

Fig. 6. Failure evolution information on BRCS with the IA of 45°.

The AE count curve has obvious multistage characteristics during the composite failure process. During the transition from the compaction and elastic stages to the plastic stage, the AE counts increase sharply, and the corresponding curve segment forms a rising phase (I). In the pre-peak plastic stage, the AE counts change stably, and the corresponding curve segment forms a stable phase (II). After peak stress, the macrocrack l_1 appears on the composite, the AE counts increase rapidly, and the corresponding curve segment forms an active phase (III). Then, the crack l_2 develops gradually while the CPB slides along the crack l_1. Because of the interaction of combined cracks, the bearing capacity of the composite decreases rapidly, and the number of AE counts first increases and then decreases sharply, and the corresponding curve segment forms a sudden change phase (IV). In the residual stress stage, the AE counts are small, and the corresponding curve segment forms a calm phase (V).

When the IA is 60° (Fig. S3), the evolution processes of

the AE point, displacement, and damage unit are similar to those of the composite with the IA of 45°. However, the locations of the AE point, damage unit, and displacement change are significant but mainly concentrated on the interface or perpendicular to the two interface cracks. The AE count curve reaches an active period after the stress peak, which shows a pulse increase or decrease mode mainly caused by the composite sliding along the nonlinear fracture interface. After the composite fracture interface slides fully, the AE counts decrease rapidly and then enter the calm area.

When the IA is 75° (Fig. S4), at the initial load stage, the deformation degree of the bottom of the CPB is greater than that of rock, accompanied by a small amount of AE. With the increase of axial displacement and fully coordinated deformation of the CPB and rock, the displacement of the composite gradually decreases from bottom to top, and the AE points and damage units mainly appear in the rock. Near the stress peak, the damage units and AE points in the upper part of the rock begin to increase, dense areas appear, and crack l_1 develops. After the stress peak, crack l_1 on the rock part expands downward, and new cracks l_2 and crack l_3 develop simultaneously. Crack l_3 runs through the CPB, whereas the upper part of crack l_2 runs through the rock and its lower part extends downward along the interface. Cracks l_2 and l_3 form an x-shaped fracture.

In the compaction and elastic stages, the AE counts are small, and the corresponding curve segment forms a quiet phase (I). In the plastic stage, the number of AE counts before the stress peak increases steadily, and the corresponding curve segment forms a rising phase (II). After the stress peak, the composite bearing capacity decreases rapidly and reaches the residual stress stage. The numerical change of the AE counts reaches a calm phase (IV) after a sudden change phase (III).

When the IA is 90° (Fig. S5), at the beginning of loading, the AE points are distributed in the CPB, and the composite displacement decreases gradually from bottom to top. With the increase of the axial displacement, sporadic damage units appear in the CPB and rock, and the AE points in the rock increase significantly. Crack l_1 develops on the rock part, the units in the corresponding area have some significant shear damage zones, and the AE points and displacement values on both sides of l_1 are different. After crack formation on the rock, the composite bearing capacity decreases rapidly. Meanwhile, crack l_2 forms along the interface, crack l_3 forms in the CPB, and an anti-N-shaped flaw forms on the composite. The multistage characteristics of the AE count curves are similar to that of the composite with an IA of 75°. The curve can also be divided into four stages.

3.5. BRCS triaxial compressive failure modes

Fig. 7 shows the failure patterns of the composite with the IAs of 45° and 60°. Their uniaxial compression failure modes are inclined plane shear failures. Their failure areas appear in the CPB of the interface, and a fracture zone is formed between the fracture plane and the interface. The fracture planes of the composites are similar regardless of CPs, a v-shaped failure is formed by the intersection of shear cracks along the upper half of the interface, and the shear cracks are perpendicular to the interface and penetrate the CPB.

The failure pattern of the composite with an IA of 75° is shown in Fig. S6(a). Its uniaxial compression failure modes

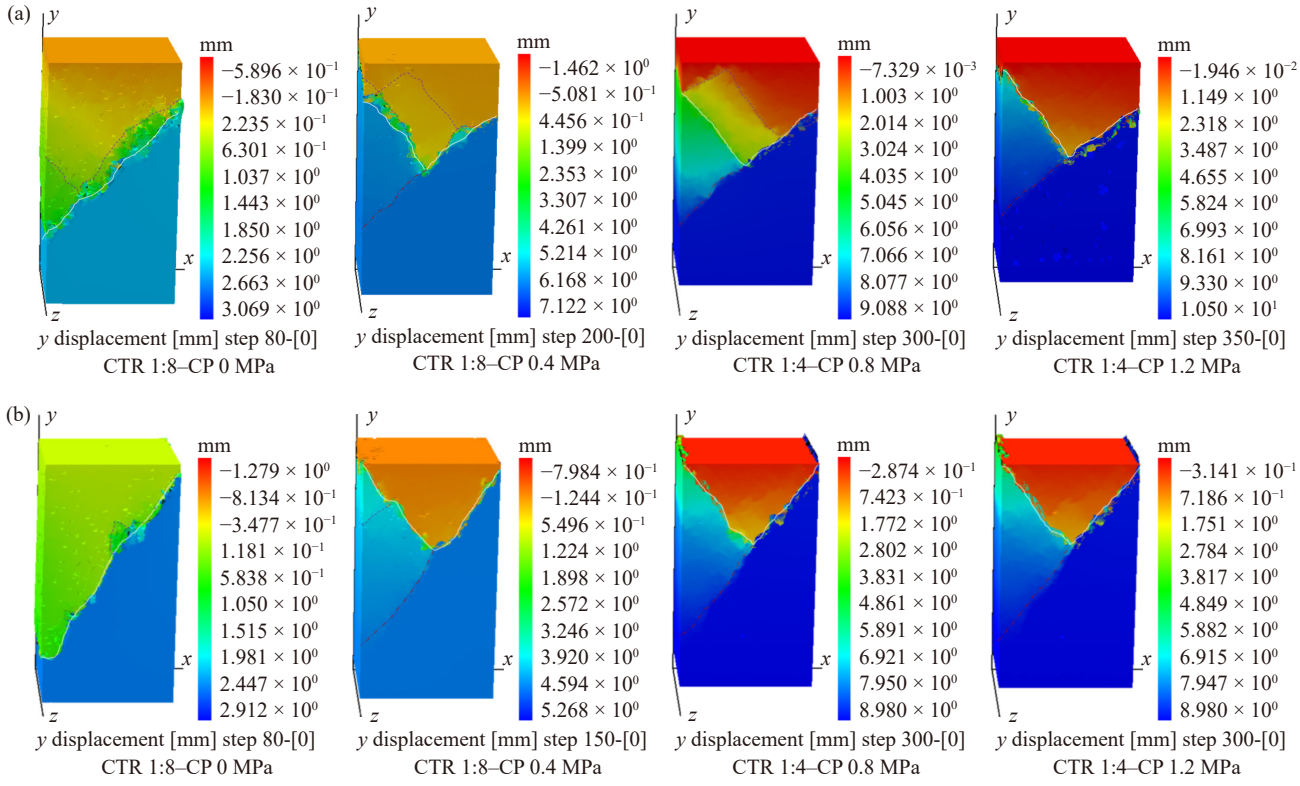

Fig. 7. BRCS triaxial compressive failure patterns: (a) IA of 45°; (b) IA of 60°.

include a compression–shear crack in the upper part of the rock and a shear crack along the interface in the CPB. The crack cross-exists to form combined shear failure. For the composite with CTR 1:8 and CP 0.4 or 0.8 MPa, a through shear crack appears on the rock, and CPB combines a shear crack along the interface to form an x-shaped conjugate shear failure. As the compression–shear crack penetrates the rock, the shear fracture surface penetrates the CPB, the shear crack extends along the lower part of the interface to form a y-shaped shear failure, and the BRCS with CTR 1:8 and CP 1.2 MPa is destroyed. For the composite with CTR 1:4, the shear crack of the rock is combined with the shear slip along the interface to form a shear fracture plane, which accompanies the formation of failure areas.

Fig. S6(b) shows the failure pattern of the composite with an IA of 90°. When the CTR is 1:8, its uniaxial compression failure mode is a shear fracture plane that penetrates the entire structure and accompanies some secondary tensile cracks in the CPB and rock in the lower part. When the CTR is 1:4, the uniaxial compression failure mode is one shear crack penetrating the rock, the other shear crack penetrating the CPB, and a slipping crack along the interface, which together form an anti-N-shaped fracture. Moreover, there are one or two secondary tensile cracks in the CPB and rock on the anti-N-shaped fracture. With the increase of CP, its failure modes are similar to that of the composite with CTR 1:4 under uniaxial compression, which appears in the middle of the model. However, no secondary cracks appear. For the angle between the shear crack throughout the composite and the axial direction, the composite with CTR 1:4 is greater than that with CTR 1:8.

The failure modes of composites with different IAs and CPs are similar. This finding shows that the failure of composites with IAs of 45° and 60° occurred in the CPB, and the failure of composites with IAs of 75° and 90° occurred in the CPB and the rock. When the IA is 45°, the slipping crack along the interface is caused by the uncoordinated deformation of the CPB and rock, which cannot accurately present the fracture angle of the composite, and the fracture plane in the CPB mirrors the fracture angle of the entire structure. When the IA is 60°, the angle of the crack propagating along the interface is similar to that of the crack in the CPB; therefore, the fracture angle takes the average of the two. When the IA is 75°, the fracture angle of the composite with CTR 1:8 is the angle of the oblique plane penetrating the composite, and the fracture angle of the composite with CTR 1:4 is the average angle of the oblique plane penetrating the rock and the sliding interface. When the IA is 90°, the composite failure is mainly controlled by the rock; thus, the angle of the shear plane in the rock is determined as the composite fracture angle. The numerical fracture angles (NFAs) of composites are obtained, as shown in Fig. 8.

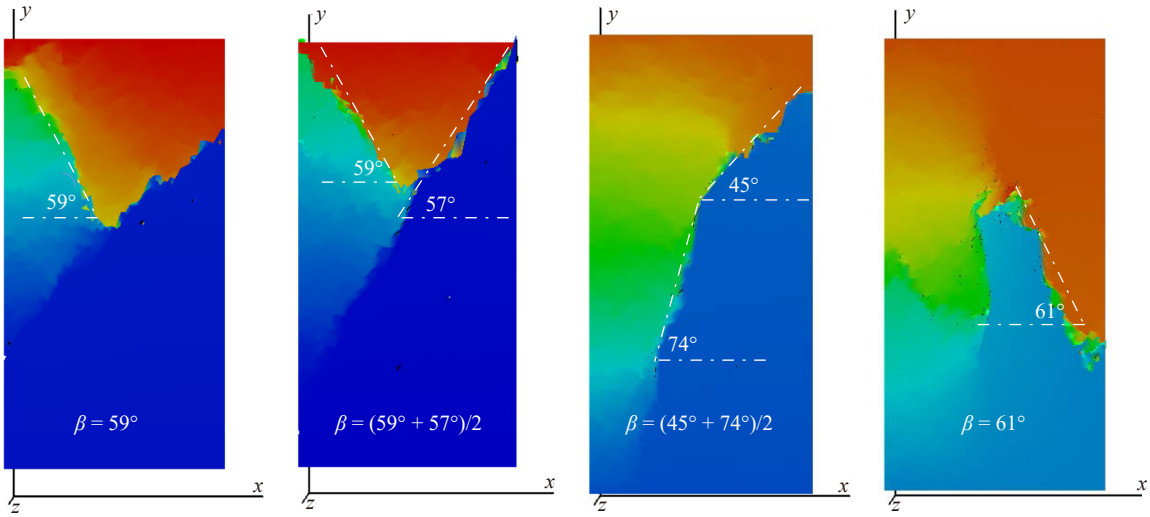

Fig. 8. BRCS triaxial compressive fracture angles.

The theoretical fracture angle (TFA) formula is expressed as Eq. (8), where β is the TFA:

$$\beta = \pi/4 + \varphi/2 \tag{8}$$

According to Table 3 and Eq. (8), the composite TFAs are obtained. The range of TFAs is between 60° and 62°, and that of NFAs is between 58° and 61°. The relative errors between them are <5%, which verifies the reliability of the numerical test.

4. Discussion

The stress models used in the triaxial compression tests can be classified into two types, namely, the IAs are less than the critical plane angle (i.e., between 45° and 60°), and the IAs are greater than the critical plane angle (i.e., between 75° and 90°). The constraints of the test models include the top section fixed and the bottom section with displacement and lateral loading ($\sigma_2 = \sigma_3$). We assumed that only elastic deformation occurs in composites under CPs. Therefore, the triaxial compression stress models of composites can be replaced by their biaxial compression stress models (Fig. 9).

The strain of the CPB and rock and interface friction of the composite can be calculated according to the static equilibrium theory, as expressed in Eqs. (9) and (10), respectively.

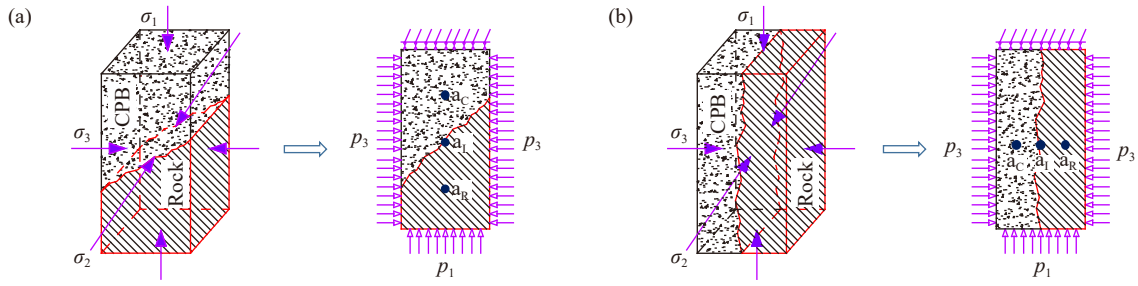

Fig. 9. BRCS triaxial compression stress analysis models: (a) the IA is less than the critical plane angle; (b) the IA is greater than the critical plane angle. a_C is the analysis point of CPB; a_I is analysis point of interface; a_R is the analysis point of rock.

$$\begin{cases} \varepsilon_{ya_c} = p_1/S_1E_C \\ \varepsilon_{ya_R} = p_1/S_1E_R \\ f_{a_I} = \mu S\left(\dfrac{p_3\cos a}{S_1} + \dfrac{p_1\cos a}{S_1}\right) \end{cases} \tag{9}$$

where ε_{ya_c} is the vertical strain of CPB, p_1 is the uniform load at the bottom section, p_3 is the uniform load at the lateral of BRCS, S_1 is the area of uniform load at the bottom section, E_C is the CPB elastic modulus, ε_{ya_R} is the rock strain, E_R is the rock elastic modulus, f_{a_I} is the interface friction, μ is the interface friction coefficient, S is the interface area, S_3 is the interface side area, and a is the interface angle.

$$\begin{cases} \varepsilon_{ya_c} = p_1/S_{1C}E_C \\ \varepsilon_{ya_R} = p_1/S_{1R}E_R \\ f_{a_I} = \mu S p_3/S_3 \end{cases} \tag{10}$$

where S_{1C} is the CPB contact area of the uniform load at the bottom section, and S_{1R} is the rock contact area of the uniform load at the bottom section.

(1) The IAs are less than the critical plane angle.

In the early stage of loading, the elastic modulus of the rock and CPB are different. Under the same load, the deformation of the CPB is greater than that of the rock. The composite shows deformation compatibility on the nonlinear interface, which causes slide failure along the contact interface, but it can be limited by the action of CP. With the increase of load, the CPB deformation reaches the plastic stage, and the shear crack penetrates the CPB. The composite failure is mainly controlled by the CPB and interface.

(2) The IAs are greater than the critical plane angle.

The bearing capacity of the rock is greater than that of the CPB. Thus, the composite failure first appears in the rock, and its failure mode is a shear failure; then, shear cracks appear in the interface and CPB. The composite failure is controlled by the CPB, rock, and interface, and the rock is the main controlling factor.

5. Conclusions

(1) The BRCS triaxial compressive stress–strain curves can be divided into five stages, namely, compaction, elasticity, yield, strain softening, and residual stress. The composite triaxial compressive strength exhibits a linear growth trend, and the CP stress strengthening effect occurs. With the increase of the IA, the CP stress strengthening effect becomes more obvious, and the change of CTR has only a slight effect on it. With the increase of the IA, the friction angle of BRCS slightly increases, and the composite cohesion changes significantly. Different CTRs have only a slight effect on composite cohesion. Relative to friction angle, cohesion is more sensitive to IA and CTR.

(2) The failure areas of BRCSs with IAs of 45° and 60° appear in the CPB of the interface, and the v-shaped failure is formed by the intersection of the shear crack along the upper half of the interface and the shear crack perpendicular to the interface through the CPB. The failure pattern of BRCSs with an IA of 75° and a CTR of 1:8 is a combined shear failure that occurs in the CPB, interface, and rock. By contrast, the failure patterns of BRCSs with an IA of 75° and a CTR of 1:4 are a shear fracture plane that occurs in the rock and interface. The failure zone of BRCS with an IA of 90° forming an anti-N-shaped fracture is composed of a shear crack penetrating the rock, a shear crack penetrating the CPB, and a slipping crack along the interface.

(3) The multistage AE count curves of BRCSs with IAs of 45° and 60° could be divided into five regions, namely, rising, quiet, active, sudden change, and calm zones, and that of BRCSs with IAs of 75° and 90° could be divided into four regions, namely, quiet, rising, sudden change, and calm zones. The mechanical characteristics of BRCSs under triaxial compression are controlled by the IA, CP, and CTR. Moreover, based on the composite static analysis models, the composite strength and failure mechanism under triaxial compression are determined. The mechanical properties of BRCSs with different nonlinear IAs were investigated through the numerical simulations of triaxial compression tests using RFPA^{3D}. By referring to relevant literature, we have proven that this research method is feasible, and the research conclusion can provide a theoretical basis for the stability analysis of backfill mining.

Acknowledgements

This work was financially supported by the National Natural Science Foundation of China (No. 51774137) and the Natural Science Foundation of Hebei Province, China (No. E2021209006).

Conflict of Interest

The authors declare no potential conflict of interest.

Supplementary Information

The online version contains supplementary material available at https://doi.org/10.1007/s12613-022-2554-9.

References

[1] Y. Wang, Z.Q. Wang, A.X. Wu, L. Wang, Q. Na, C. Cao, and G.F. Yang, Experimental research and numerical simulation of the multi-field performance of cemented paste backfill: Review and future perspectives, *Int. J. Miner. Metall. Mater.*, 30(2023), No. 2, p. 193.

[2] G.L. Xue, E. Yilmaz, W.D. Song, and S. Cao, Mechanical, flexural and microstructural properties of cement–tailings matrix composites: Effects of fiber type and dosage, *Composites Part B*, 172(2019), p. 131.

[3] E. Yilmaz, Stope depth effect on field behaviour and performance of cemented paste backfills, *Int. J. Min. Reclam. Environ.*, 32(2018), No. 4, p. 273.

[4] T. Deschamps, M. Benzaazoua, and B. Bussière, Laboratory study of surface paste disposal for sulfidic tailings: Physical model testing, *Miner. Eng.*, 24(2011), No. 8, p. 794.

[5] L. Li and P.Y. Yang, A numerical evaluation of continuous backfilling in cemented paste backfilled stope through an application of wick drains, *Int. J. Min. Sci. Technol.*, 25(2015), No. 6, p. 897.

[6] H.J. Lu, C.C. Qi, Q.S. Chen, D.Q. Gan, Z.L. Xue, and Y.J. Hu, A new procedure for recycling waste tailings as cemented paste backfill to underground stopes and open pits, *J. Clean. Prod.*, 188(2018), p. 601.

[7] C.C. Qi, Big data management in the mining industry, *Int. J. Miner. Metall. Mater.*, 27(2020), No. 2, p. 131.

[8] B.D. Thompson, W.F. Bawden, and M.W. Grabinsky, *In situ* measurements of cemented paste backfill at the Cayeli Mine, *Can. Geotech. J.*, 49(2012), No. 7, p. 755.

[9] T. Yılmaz, B. Ercikdi, and H. Deveci, Utilisation of construction and demolition waste as cemented paste backfill material for underground mine openings, *J. Environ. Manage.*, 222(2018), p. 250.

[10] I.L.S. Libos and L. Cui, Effects of curing time, cement content, and saturation state on mode-I fracture toughness of cemented paste backfill, *Eng. Fract. Mech.*, 235(2020), art. No. 107174.

[11] G.L. Xue and E. Yilmaz, Strength, acoustic, and fractal behavior of fiber reinforced cemented tailings backfill subjected to triaxial compression loads, *Constr. Build. Mater.*, 338(2022), art. No. 127667.

[12] Z.Y. Zhao, S. Cao, and E. Yilmaz, Effect of layer thickness on the flexural property and microstructure of 3D-printed rhomboid polymer-reinforced cemented tailing composites, *Int. J. Miner. Metall. Mater.*, 30(2023), No. 2, p. 236.

[13] H.Q. Jiang, M. Fall, E. Yilmaz, Y.H. Li, and L. Yang, Effect of mineral admixtures on flow properties of fresh cemented paste backfill: Assessment of time dependency and thixotropy, *Powder Technol.*, 372(2020), p. 258.

[14] E. Sadrossadat, H. Basarir, G.H. Luo, A. Karrech, R. Durham, A. Fourie, and M.Elchalakani, Multi-objective mixture design of cemented paste backfill using particle swarm optimisation algorithm, *Miner. Eng.*, 153(2020), art. No. 106385.

[15] N.F. Liu, L. Cui, and Y. Wang, Analytical assessment of internal stress in cemented paste backfill, *Adv. Mater. Sci. Eng.*, 2020(2020), art. No. 6666548.

[16] M. Fall and M. Pokharel, Coupled effects of sulphate and temperature on the strength development of cemented tailings backfills: Portland cement-paste backfill, *Cem. Concr. Compos.*, 32(2010), No. 10, p. 819.

[17] S. Cao, W.D. Song, and E. Yilmaz, Influence of structural factors on uniaxial compressive strength of cemented tailings backfill, *Constr. Build. Mater.*, 174(2018), p. 190.

[18] E. Yilmaz, T. Belem, and M. Benzaazoua, Specimen size effect on strength behavior of cemented paste backfills subjected to different placement conditions, *Eng. Geol.*, 185(2015), p. 52.

[19] Y.R. Wang, H.J. Lu, and J. Wu, Experimental investigation on strength and failure characteristics of cemented paste backfill–rock composite under uniaxial compression, *Constr. Build. Mater.*, 304(2021), art. No. 124629.

[20] M.L. Walske, H. McWilliam, J. Doherty, and A.Fourie, Influence of curing temperature and stress conditions on mechanical properties of cementing paste backfill, *Can. Geotech. J.*, 53(2016), No. 1, p. 148.

[21] Z.M. Huang, Z.G. Ma, L. Zhang, P. Gong, Y.K. Zhang, and F. Liu, A numerical study of macro-mesoscopic mechanical properties of gangue backfill under biaxial compression, *Int. J. Min. Sci. Technol.*, 26(2016), No. 2, p. 309.

[22] D. Martogi and S. Abedi, Microscale approximation of the elastic mechanical properties of randomly oriented rock cuttings, *Acta Geotech.*, 15(2020), No. 12, p. 3511.

[23] X.S. Li, Y.C. Li, and S.S. Wu, Experimental investigation into the influences of weathering on the mechanical properties of sedimentary rocks, *Geofluids*, 2020(2020), art. No. 8893299.

[24] S. Durmaz and D. Ülgen, Prediction of earthquake-induced permanent deformations for concrete-faced rockfill dams, *Nat. Hazards*, 105(2021), No. 1, p. 587.

[25] M. Bost, H. Mouzannar, F. Rojat, G. Coubard, and J.P. Rajot, Metric scale study of the bonded concrete-rock interface shear behaviour, *KSCE J. Civ. Eng.*, 24(2020), No. 2, p. 390.

[26] V.N. Aptukov and S.V. Volegov, Modeling concentration of residual stresses and damages in salt rock cores, *J. Min. Sci.*, 56(2020), No. 3, p. 331.

[27] R.J. Clément, Z. Lun, and G.Ceder, Cation-disordered rocksalt transition metal oxides and oxyfluorides for high energy lithium-ion cathodes, *Energy Environ. Sci.*, 13(2020), No. 2, p. 345.

[28] Q. Ma, Y.L. Tan, X.S. Liu, Q.H. Gu, and X.B. Li, Effect of coal thicknesses on energy evolution characteristics of roof rock–coal–floor rock sandwich composite structure and its damage constitutive model, *Composites Part B*, 198(2020), art. No. 108086.

[29] Y.R. Yang, X.P. Lai, P.F. Shan, and F. Cui, Comprehensive analysis of dynamic instability characteristics of steeply inclined coal-rock mass, *Arab. J. Geosci.*, 13(2020), No. 6, art. No. 241.

[30] K. Wang, F. Du, X. Zhang, L. Wang, and C.P. Xin, Mechanical properties and permeability evolution in gas-bearing coal-rock combination body under triaxial conditions, *Environ. Earth Sci.*, 76(2017), No. 24, art. No. 815.

[31] N.J.F. Koupouli, T. Belem, P. Rivard, and H. Effenguet, Direct shear tests on cemented paste backfill–rock wall and cemented paste backfill–backfill interfaces, *J. Rock Mech. Geotech. Eng.*, 8(2016), No. 4, p. 472.

[32] Y. Zhang, Z.H. Zhang, L.J. Guo, and X.L. Du, Strength model of backfill–rock irregular interface based on fractal theory, *Front. Mater.*, 8(2021), art. No. 792014.

[33] Z.G. Xiu, S.H. Wang, Y.C. Ji, F.L. Wang, F.Y. Ren, and V.T. Nguyen, The effects of dry and wet rock surfaces on shear behavior of the interface between rock and cemented paste backfill, *Powder Technol.*, 381(2021), p. 324.

[34] N. Falaknaz, M. Aubertin, and L. Li, Numerical investigation of the geomechanical response of adjacent backfilled stopes, *Can. Geotech. J.*, 52(2015), No. 10, p. 1507.

[35] W.B. Xu, Y. Cao, and B.H. Liu, Strength efficiency evaluation of cemented tailings backfill with different stratified structures, *Eng. Struct.*, 180(2019), p. 18.

[36] W.L. Wu, W.B. Xu, and J.P. Zuo, Effect of inclined interface

angle on shear strength and deformation response of cemented paste backfill–rock under triaxial compression, *Constr. Build. Mater.*, 279(2021), art. No. 122478.

[37] C.A. Tang, and P.K. Kaiser, Numerical simulation of cumulative damage and seismic energy release during brittle rock failure—Part I: Fundamentals, *Int. J. Rock Mech. Min. Sci.*, 35(1998), No. 2, p. 113.

[38] K. Ma, C.A. Tang, Z.Z. Liang, D.Y. Zhuang, and Q.B. Zhang, Stability analysis and reinforcement evaluation of high-steep rock slope by microseismic monitoring, *Eng. Geol.*, 218(2017), p. 22.

[39] S.Y. Wang, S.W. Sloan, M.L. Huang, and C.A. Tang, Numerical study of failure mechanism of serial and parallel rock Pillars, *Rock Mech. Rock Eng.*, 44(2011), No. 2, p. 179.

[40] P. Liang and H.J. Lu, Mechanical behaviour and failure characteristics of cemented paste backfill under lateral unloading condition, *Int. J. Min. Miner. Eng.*, 11(2020), No. 1, art. No. 66.

[41] Z.Z. Liang, H. Xing, S.Y. Wang, D.J. Williams, and C.A. Tang, A three-dimensional numerical investigation of the fracture of rock specimens containing a pre-existing surface flaw, *Comput. Geotech.*, 45(2012), p. 19.

[42] B.Q. Li and H.H. Einstein, Comparison of visual and acoustic emission observations in a four point bending experiment on barre granite, *Rock Mech. Rock Eng.*, 50(2017), No. 9, p. 2277.

[43] C.A. Tang, H. Liu, P.K.K Lee, Y. Tsui, and L. Tham, Numerical studies of the influence of microstructure on rock failure in uniaxial compression—Part I: Effect of heterogeneity, *Int. J. Rock Mech. Min. Sci.*, 37(2000), No. 4, p. 555.

[44] W.C. Zhu and C.A. Tang, Micromechanical model for simulating the fracture process of rock, *Rock Mech. Rock Eng.*, 37(2004), No. 1, p. 25.

[45] G. Li and C.A. Tang, A statistical meso-damage mechanical method for modeling trans-scale progressive failure process of rock, *Int. J. Rock Mech. Min. Sci.*, 74(2015), p. 133.

[46] X.M. Wei, L.J. Guo, X.L. Zhou, C.H. Li, and L.X. Zhang, Full sequence stress evolution law and prediction model of high stage cemented backfill, *Rock Soil Mech.*, 41(2020), No. 11, p. 3613.